A printed proximity-sensing surface based on organic pyroelectric sensors and organic thin-film transistor electronics

nature electronics

ARTICLES

https://doi.org/10.1038/s41928-022-00762-6

Check for updates

A printed proximity-sensing surface based on organic pyroelectric sensors and organic thin-film transistor electronics

Marco Fattori[1,2]✉, Simone Cardarelli[1,2], Joost Fijn[1,3], Pieter Harpe[1], Micael Charbonneau[4], Denis Locatelli[4], Stephanie Lombard[4], Christelle Laugier[4], Laurent Tournon[4], Stephanie Jacob[4], Krunoslav Romanjek[4], Romain Coppard[4], Herbert Gold[5], Manfred Adler[5], Martin Zirkl[5], Jonas Groten[5], Andreas Tschepp[5], Bernhard Lamprecht[5], Markus Postl[5], Barbara Stadlober[5], Josephine Socratous[6] and Eugenio Cantatore[1]

Large-area, flexible proximity-sensing surfaces are useful in a range of applications including process control, work security and robotics. However, current systems typically require rigid and thick electronics, which limit how they can be used. Here we report a flexible large-area proximity-sensing surface fabricated using printed organic materials and incorporating analogue front-end electronics in each pixel. The sensing surface is built with printed thin-film pyroelectric sensors based on poly(vinylidene fluoride-co-trifluoroethylene) co-polymers and printed organic thin-film transistors. A 5×10 matrix front-plane, consisting of long-wavelength infrared organic pyroelectric sensors, is laminated with an organic transistor analogue front-end backplane. The electronic front end provides sensor-signal amplification and pixel addressing to maximize the detection distance and reduce pixel crosstalk. An average yield of 82% fully working pixels for the backplane and a maximum system yield of 96%, which corresponds to 768 defect-free devices, are achieved. The system can detect a human hand approaching from different directions and track the position of a movable heat source up to a distance of around 0.4 m at a readout speed of 100 frames per second.

Recent advances in printed electronics have made it possible to use organic materials to fabricate flexible and stretchable electronic skins (e-skins) for human–machine interface and human–robot interaction (HRI) applications (Fig. 1a)[1–8]. Organic materials can be processed at low temperatures and on lightweight and mechanically flexible plastic substrates, which can be shaped into a wide range of form factors. Printing techniques can be used to create sensing elements that cover large-area surfaces and costs can be kept low, providing a major advantage over conventional silicon-based systems. Furthermore, the availability of new pyroelectric sensing materials can extend the sensing capabilities of e-skins to temperature and proximity sensing[5,8,9], making them potentially useful in HRI safety applications such as collision avoidance[10–13]. Industrial manipulators typically operate for safety reasons in environments separated from human workers. The use of proximity-sensing e-skins could, for example, relax the need for physical separation between robots and humans (Fig. 1a), even in unstructured environments, leading to cost reduction and more efficient HRI in industry[14].

These features make use of functional organic materials attractive from the application point of view. However, only a few large-area sensing surface arrays with embedded active front-end electronics (AFE)—fabricated using either photolithography processes[3,4] or printing techniques[6,8]—have been demonstrated. In some of these demonstrations, the front-end electronics provides only active-matrix addressing of the sensor elements[3,6,8]. From the architecture perspective, active-matrix addressing solutions are preferred to passive ones as they can provide better isolation between sensing pixels. This leads to unambiguous sensor selection, which makes post-processing of the acquired data easier. To fully exploit these advantages, technologies such as organic thin-film transistors (OTFT) with high on-current (I_{ON}) off-current (I_{OFF}) ratio and good noise performance are needed.

Although simple and effective, active-matrix addressing schemes have some limitations. Sensing surfaces distributed over large areas are intrinsically susceptible to coupling with interferers, which can introduce substantial errors in the reconstruction process. Issues also arise when printed electronics are used with sensors producing a charge signal, as the large OTFT feature sizes can introduce unwanted effects related to switching, such as charge injection and clock feedthrough. In addition, the large parasitic capacitance of the matrix interconnects can lower signal voltage amplitudes, resulting in decreased signal-to-noise ratio (SNR). These limitations can be mitigated by using AFE in each pixel at the cost of higher circuit complexity (in terms of number of devices). The integration of AFE in the pixel matrix can be used to achieve sensor-signal amplification, improve immunity to interference and pixel crosstalk, and enhance the achievable SNR. To enable this, an OTFT technology featuring high device yield and a circuit architecture that is robust against transistor parameter variability should be used.

In this Article, we report a sensing surface that can be used for infrared (IR) human proximity detection, and is fabricated with printed organic materials and equipped with an AFE in each pixel. The proximity detection is achieved using printed thin-film pyroelectric

[1]Eindhoven University of Technology, Department of Electrical Engineering, Eindhoven, The Netherlands. [2]MicroAlign, Eindhoven, The Netherlands. [3]TNO, Eindhoven, The Netherlands. [4]CEA-LITEN, Grenoble, France. [5]Joanneum Research, Graz, Austria. [6]FlexEnable, Cambridge, UK. ✉e-mail: m.fattori@tue.nl

sensors based on poly(vinylidene fluoride-co-trifluoroethylene) (PVDF–TrFE) co-polymers[8] and the electronics is manufactured using state-of-the-art printed OTFT technology[9].

Printed proximity-sensing surface. Our system consists of a printed proximity-sensing surface, line-addressing module and silicon readout electronics. A suggested robotic safety application is shown in Fig. 1a and the simplified block diagram of the system is shown in Fig. 1b. The sensing surface is a matrix of pixels, each including a sensor, AFE and addressing, which enable IR human proximity detection. The pixels in a row can be selected by a dedicated line driver module[9,15–19], which could also be manufactured with OTFTs[9] to minimize the number of interconnections with the silicon readout electronics. Here, however, this part of the system as well as the electronics for the sensor matrix readout and digitalization are implemented with off-the-shelf silicon components.

The proximity-sensing surface has a system-on-foil design built by the lamination of a matrix of proximity sensors printed on a plastic substrate (frontplane) with a second plastic sheet (backplane) containing a matching matrix of printed OTFT electronics, which performs addressing and signal amplification (AFE) functions. This approach allows to relax the fabrication process constraints for both sensors and electronics, as well as preserving the mechanical flexibility of the final assembly.

The sensors used for human proximity sensing in the frontplane are based on pyroelectric materials. Several works have demonstrated that pyroelectric detectors can be fabricated by using poly(vinylidene fluoride) (PVDF) polymers[20–22], alone or in combination with trifluoroethylene (TrFE), leading to ferroelectric PVDF–TrFE co-polymers[5,8,23,24]. Owing to their higher pyroelectric coefficient compared with other polymers, fast response and processability from solutions, PVDF–TrFE co-polymers are well suited to low-cost large-area array implementations of long-wavelength infrared (LWIR) sensors. The sensors absorb LWIR radiation of wavelengths between 8 and 14 µm, which leads to temperature changes in the pyroelectric material. They only respond to time-dependent temperature variations ΔT, which are converted into an electrical charge ΔQ owing to the pyroelectric response of co-polymer crystallites that are aligned by poling[8]. The limitation of the detection mechanism to time-varying signals does not reduce the usability of these sensors in the target applications, since proximity detection is typically associated with moving heat sources. In this work, the sensing frontplane is based on printed pyroelectric detectors (Joanneum Research[8]). The manufacturing process used to fabricate the sensors, their layer stack and the photograph of a typical device are described in Supplementary Fig. 1a,b.

The backplane electronics enabling the readout of the sensor frontplane is designed by using the analytical thermal and electrical model of the pyroelectric sensor provided elsewhere[25], which describes the relationship between the IR radiation absorbed and the corresponding charge (or current) generated.

The charge ΔQ_S generated across the detector by the absorbed incident IR radiation[25] is proportional to the temperature change ΔT_{PVDF} of the pyroelectric material between the top and bottom electrodes. The expression for ΔQ_S in the angular frequency domain is

$$\Delta Q_S(j\omega) = p_{pyro} A_S \Delta T_{PVDF}, \quad (1)$$

where p_{pyro} and A_S are the pyroelectric coefficient and active area of the detector, respectively. The expression of the current signal I_S generated by the sensor can be obtained from equation (1) using the model provided elsewhere[25]. The resulting expression of I_S is

$$I_S(j\omega) = j\omega \frac{p_{pyro} A_S \eta P}{G_T + j\omega H}, \quad (2)$$

where P is the IR incident power on the detector; η is the emissivity of the pyroelectric element (which accounts for the fraction of radiation power absorbed by the detector); ω is the angular frequency; and H and G_T are the heat capacitance and thermal conductance of the sensor, respectively. Interestingly, equation (2) reveals that the pyroelectric sensor can be electrically modelled with a current source that produces a non-zero output signal only if subject to a time-varying excitation. To account for the frequency-dependent impedance of the sensor, its electrical model also includes a capacitance C_E and leakage conductance G_E, connected in parallel to the current source I_S.

Finally, the sensitivity of detector R_I can be derived from equation (2) and expressed in terms of current responsivity as described elsewhere as[25]

$$R_I = \left|\frac{I_S}{P}\right| = \frac{p_{pyro} A_S \eta \omega}{G_T \sqrt{1 + (\omega H/G_T)^2}}. \quad (3)$$

Supplementary Table 1 lists the main parameters of the pyroelectric sensor used in this work.

The gravure-printed OTFT technology used in this work[9] to manufacture the backplane circuits is developed at CEA Liten on the PICTIC pilot line, using GEN1 sheet-based process in a cleanroom environment (500 m²; class, 10,000). Since interface quality and overlay control are critical in OTFTs, a sheet-to-sheet strategy on a glass carrier is exploited in this fabrication process, enabling high versatility, easier control of surface treatments and improved registration performance. The detailed description of the fabrication process, transistor layer stack and micrograph of a typical manufactured device are provided in the Supplementary Information and Supplementary Fig. 1c–e. Additional details on the electric characteristics of the OTFTs and their uniformity are also provided in the Supplementary Information.

System-on-foil design. In this section, the design of each part of the system-on-foil proximity-sensing surface is discussed. The first design step is the definition of the number of matrix elements and their physical dimensions. Next, a multiplexing strategy for sensor aggregation is investigated, and the system timing specifications are derived. Afterwards, the AFE architecture is selected, and the main front-end specifications are defined. At this stage, an analytical noise model is used to choose the size of the sensor active area. In the last part of this section, the design of an IR-guiding funnel array to enhance the directivity and increase the sensitivity of the pyroelectric sensors is discussed.

The core of the proposed system architecture is the active matrix of pyroelectric sensors. The proposed active matrix employs 5 (rows) × 10 (columns) elements arranged with a pitch of 1 cm in both directions on a 5 × 10 cm² area. The chosen spatial resolution of the matrix is comparable to earlier e-skins reported in the literature for target HRI applications[26–28].

The elements of the matrix are multiplexed to fully exploit the advantages of the distributed OTFT electronics. This strategy allows to reduce the number of interconnections with the silicon readout electronics, enabling potential upscaling of the sensing surface. A time-division multiplexing (TDM) approach has been chosen here due to its simplicity in terms of transistor count. To enable TDM, the backplane electronics is equipped with an analogue multiplexer (AMUX). This is driven by the external line driver circuitry (Fig. 1c). The implementation of AMUX is very minimalistic and requires only a pass-gate transistor in each pixel (Fig. 1c,h). The simplicity of circuit implementation introduces a trade-off for the TDM between the number of aggregated elements and noise level, which limits the achievable SNR. Indeed, to aggregate more elements within the same matrix frame time, the switching speed of the multiplexer should increase. However, since the sensor noise is wideband, if no

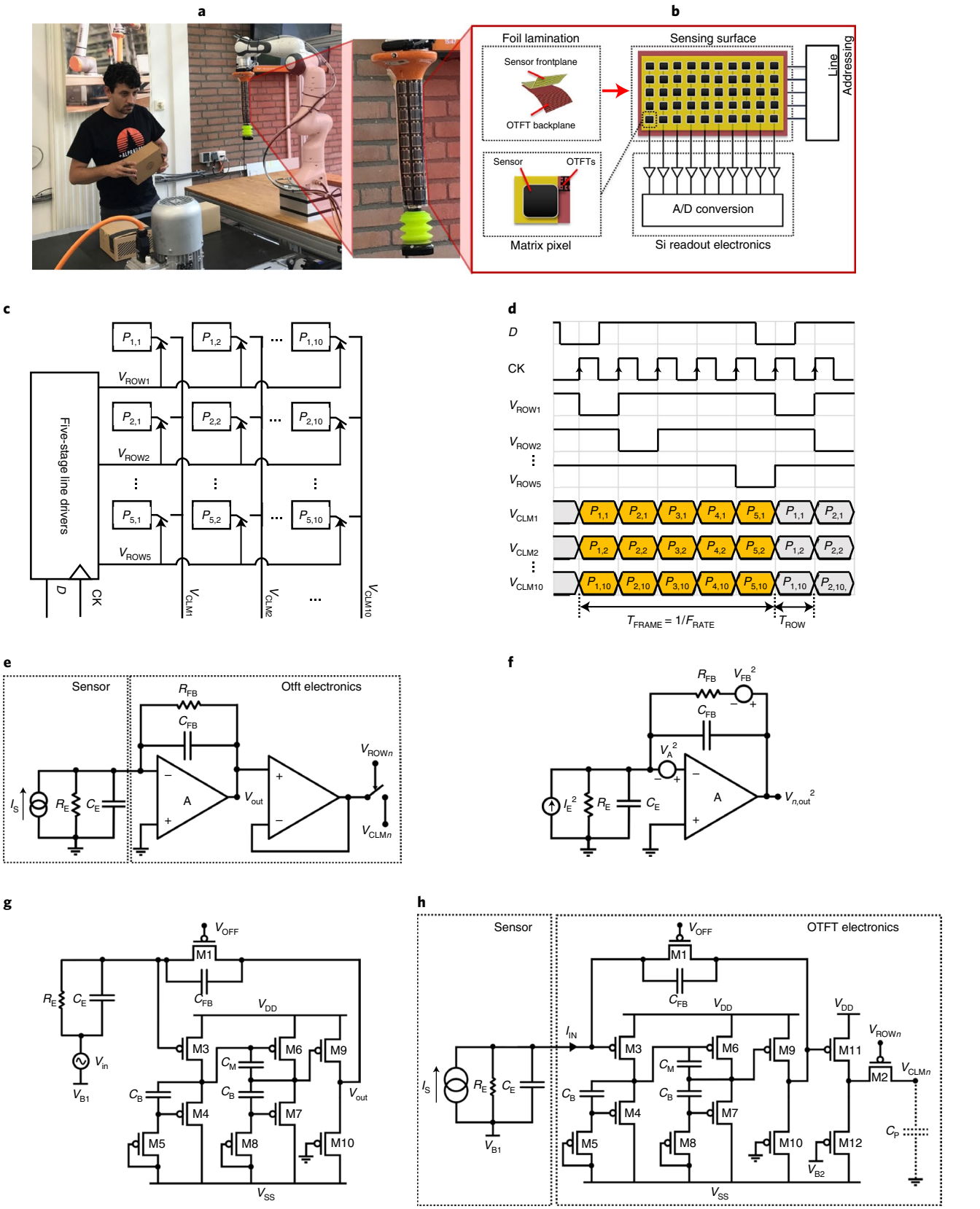

Fig. 1 | Proposed proximity-sensing surface. a, Potential application of the proposed proximity-sensing surface. The sensing surface can be shaped to cover a robotic arm and used to improve safety (collision avoidance) in HRI applications. **b**, Block diagram of the proposed system comprising the printed proximity-sensing surface, silicon readout electronics and line-addressing module. **c**, TDM architecture used in the proposed proximity-sensing surface. **d**, Simplified time diagram of the matrix readout. **e**, Block-level schematic of the proposed backplane pixel. **f**, Equivalent noise model for the analysis of the front-end noise performance. **g**, Front-end connected as a voltage amplifier with the feedback network (M1, C_{FB}) also used in the closed-loop CSA configuration. **h**, Transistor-level implementation of the proposed backplane pixel.

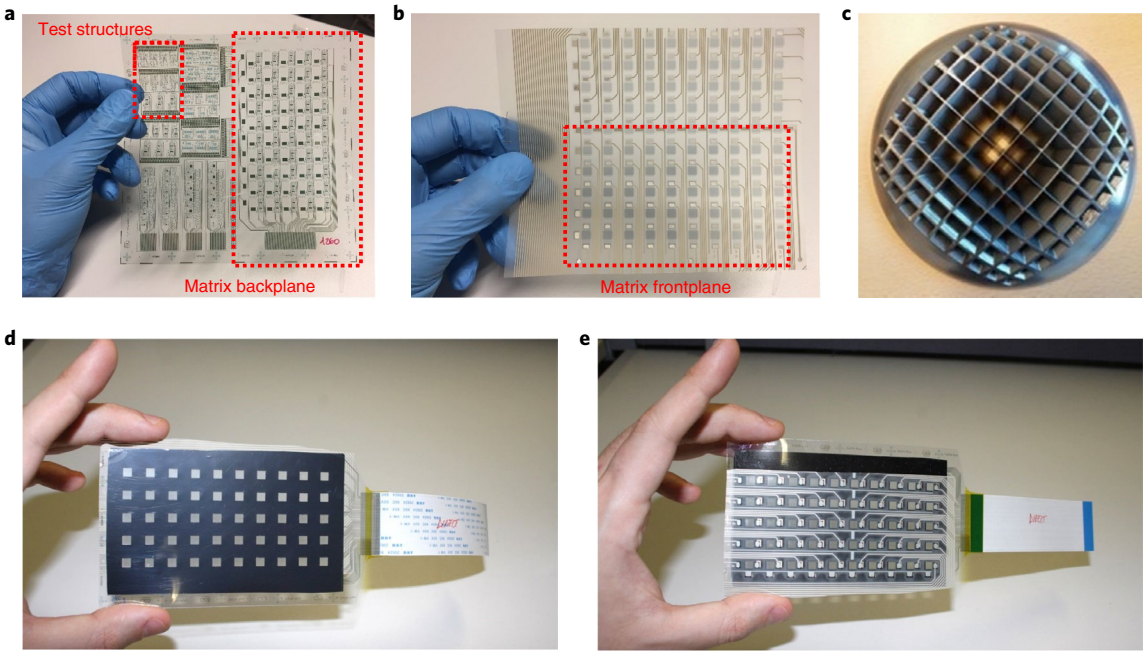

Fig. 2 | Prototype of a proximity-sensing surface. a, Fabricated module comprising the backplane matrix electronics and AFE test structures. **b**, Manufactured array of pyroelectric sensors forming the matrix sensing frontplane. **c**, Three-dimensional printed funnel array after metallization coating. **d**,**e**, Proximity-sensing surface obtained after the lamination process: front view (**d**) and back view (**e**).

antialiasing filter is introduced before the multiplexing, the higher switching speed (and thus the bandwidth needed) would lead to a higher noise level. It is also clear that in this architecture, all the pass-gate transistors operate at the same switching speed, which could become extremely demanding for OTFTs if many sensor elements need to be aggregated at relatively high frame rates.

In the proposed architecture, the sensors are grouped into five rows. The sensing elements in a row are read in parallel using a column bus ($V_{CLM1...10}$; Fig. 1c). The matrix rows are sequentially scanned and the ten columns are simultaneously recorded, as shown in a simplified timing diagram (Fig. 1d).

Pyroelectric sensors employed in proximity detection applications are typically read at a sampling rate in the hertz range[8,26]. Similarly, in this work, the bandwidth of interest for proximity sensing has been assumed to be between 1 and 10 Hz. A matrix-readout frame rate F_{RATE} as high as 100 frames per second has been targeted to prove the potential for future upscaling of the system-on-foil design.

The potential noise issue introduced by TDM aggregation can be mitigated by introducing AFE in each pixel, which further provides local signal amplification, filtering before the multiplexer and decouples the sensor from the readout stage placed after the AMUX.

In this work, each pyroelectric sensor is continuously readout in the current mode by means of a dedicated charge-sensitive amplifier (CSA) (Fig. 1e,h). Owing to the virtual ground provided by the CSA, the charge generated by the sensor can be collected on feedback capacitance C_{FB}; as C_{FB} is smaller than the sensor capacitance C_E, amplification of the sensor voltage is enabled. In addition, the CSA inherently integrates the input signal, leading to an output voltage proportional to the charge generated by the sensor and enabling proximity detection based on signal amplitude. A voltage buffer (Fig. 1e) is also placed between the CSA and TDM switch to shield capacitor C_{FB} from unwanted charge injection occurring during active-matrix addressing. Owing to the signal amplification provided by the CSA, the impact of noise contributions from the voltage buffer and successive stages of conditioning chain can be considered negligible. To achieve this, a signal voltage amplification of $\alpha = 10$ in the CSA is assumed to be sufficient. As a consequence, the ratio between the sensor and CSA feedback capacitance is set to α. Moreover, for the correct functionality of the CSA, its core amplifier must provide an open-loop gain of $A \gg \alpha$. Thus, an additional requirement for the design of the CSA is a minimum core amplifier gain of $A = 50$ V/V.

An analytical study of the front-end noise performance is required to choose the size of the sensor active area. An equivalent noise model of the sensor and front-end electronics has been derived (Fig. 1f) following the approach provided elsewhere[29]. In detail, I_E^2 is the wideband noise-current contribution associated with electrical leakage conductance of the sensor, V_A^2 represents the voltage-input-referred noise power spectral density of the core amplifier and V_{FB}^2 is the wideband noise-voltage component related to resistance R_{FB}. The noise contribution associated with the thermal agitation of charges in the pyroelectric material has not been considered here, since this is typically negligible compared with the other noise sources of the sensor[25]. From an inspection of the circuit shown in Fig. 1f, it is possible to derive an approximated expression of the in-band output-referred noise power spectral density $V_{n,out}^2$:

$$V_{n,out}^2 \cong \frac{A^2}{(1+A)^2}\left(V_A^2\left(1+\frac{C_E}{C_{FB}}\right)^2+\left(V_{FB}^2+R_{FB}^2 I_E^2\right)\left|\frac{1}{1+j2\pi f R_{FB}C_{FB}}\right|^2\right), \quad (4)$$

where $R_E = 1/G_E$. By integrating equation (4) over frequency f and by introducing expressions of the power spectral density for I_E^2 and V_{FB}^2 according to the Johnson–Nyquist formulation[30], it is possible to calculate the integrated output-referred noise power $\overline{V_{n,out}^2}$ of the front end. The equivalent noise charge power at the output, $\overline{Q_{n,out}^2}$, can then be computed as

$$\overline{Q_{n,out}^2} = \overline{V_{n,out}^2}\, C_{FB}^2 = \frac{A^2}{(1+A)^2}\left(\overline{V_A^2}\,(C_{FB}+C_E)^2 + k_B T\, C_{FB}\left(1+\frac{R_{FB}}{R_E}\right)\right), \quad (5)$$

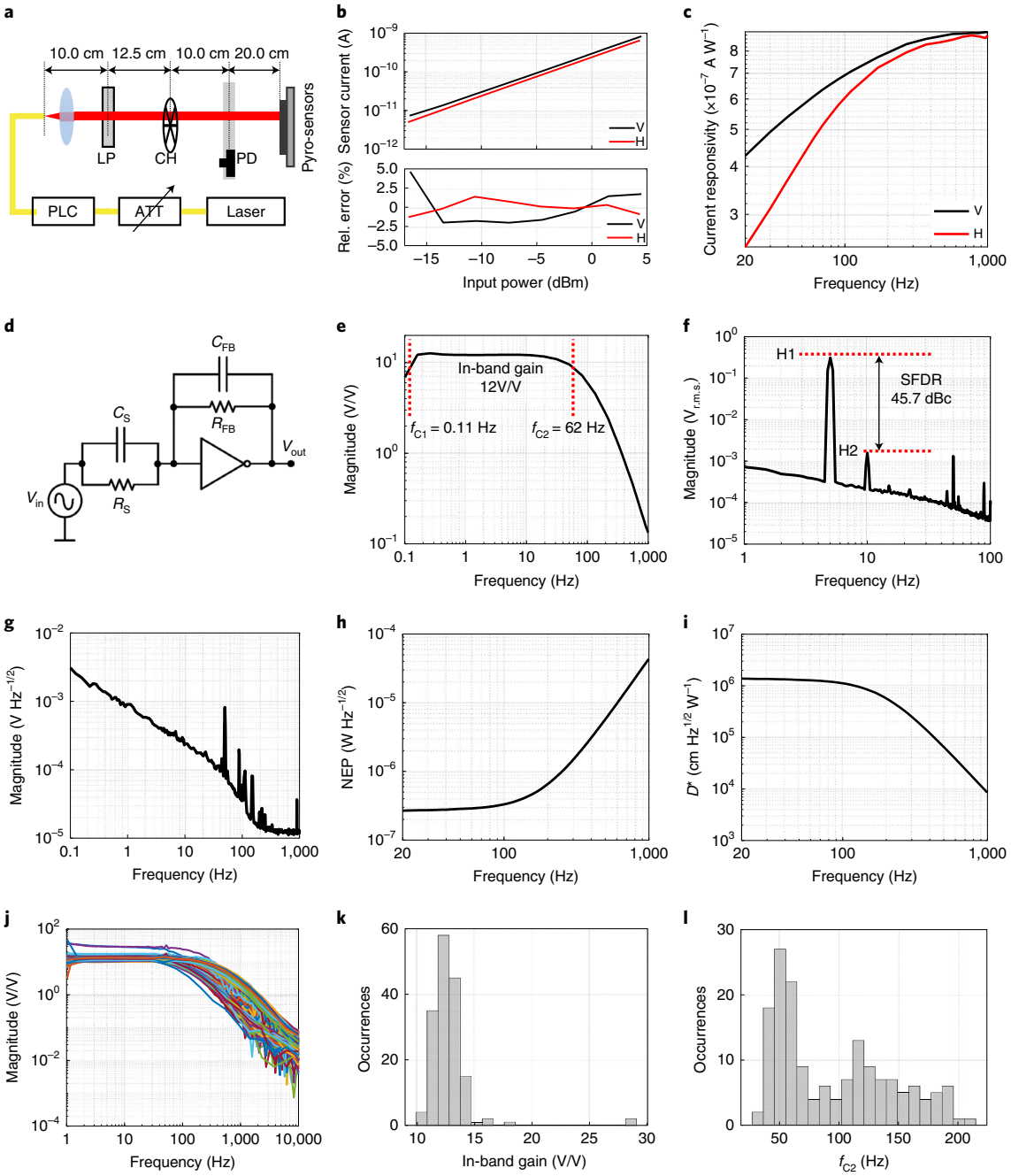

Fig. 3 | Pyroelectric sensor characterization. a, Simplified diagram (top view) of the measurement setup. **b**, Sensor current response versus input IR power for horizontal (H, red) and vertical (V, black) IR polarizations and their relative linearity error extracted from best-fit linear regressions. **c**, Sensor current responsivity at H (red) and V (black) IR polarizations. Electrical performance evaluation of the AFE. **d**, Simplified schematic of the CSA connected as a voltage amplifier. **e**, Measured frequency response of the voltage amplifier. **f**, Recorded output spectrum of the voltage amplifier (25 $mV_{r.m.s.}$ single-tone input at 5 Hz; Hanning window; averaging factor, 100). **g**, Output-referred noise-voltage spectral density. **h**, NEP of the detector (including sensor and front end). **i**, Corresponding specific detectivity (including sensor and front end). Electrical performance evaluation of the backplane pixels. **j**, Frequency responses recorded from the 163 working pixels connected as voltage amplifiers. **k**, Histogram of the in-band gain distribution: mean value $\mu = 12.7$ V/V and standard deviation $\sigma = 2.0$ V/V (15.7% of the mean value). **l**, Histogram of the amplifier second cut-off frequency f_{C2} distribution: mean value, $\mu = 96.0$ Hz and standard deviation $\sigma = 48.5$ Hz (50.7% of the mean value).

where k_B is the Boltzmann constant, T is the temperature (in kelvin) and $\overline{V_A^2}$ is the integrated input-referred noise of the core amplifier. The term $\frac{A^2}{(1+A)^2}$ is always smaller than 1, and therefore, the following upper bound can be defined for the equivalent output noise charge.

$$\overline{Q_{n,\mathrm{out}}^2} \leq \overline{V_A^2}\,(C_{\mathrm{FB}} + C_{\mathrm{E}})^2 + \left(1 + \frac{R_{\mathrm{FB}}}{R_{\mathrm{E}}}\right) k_B T\, C_{\mathrm{FB}} \qquad (6)$$

The achievable SNR can be calculated by integrating equation (2) over frequency to obtain the input signal charge Q_S. Considering

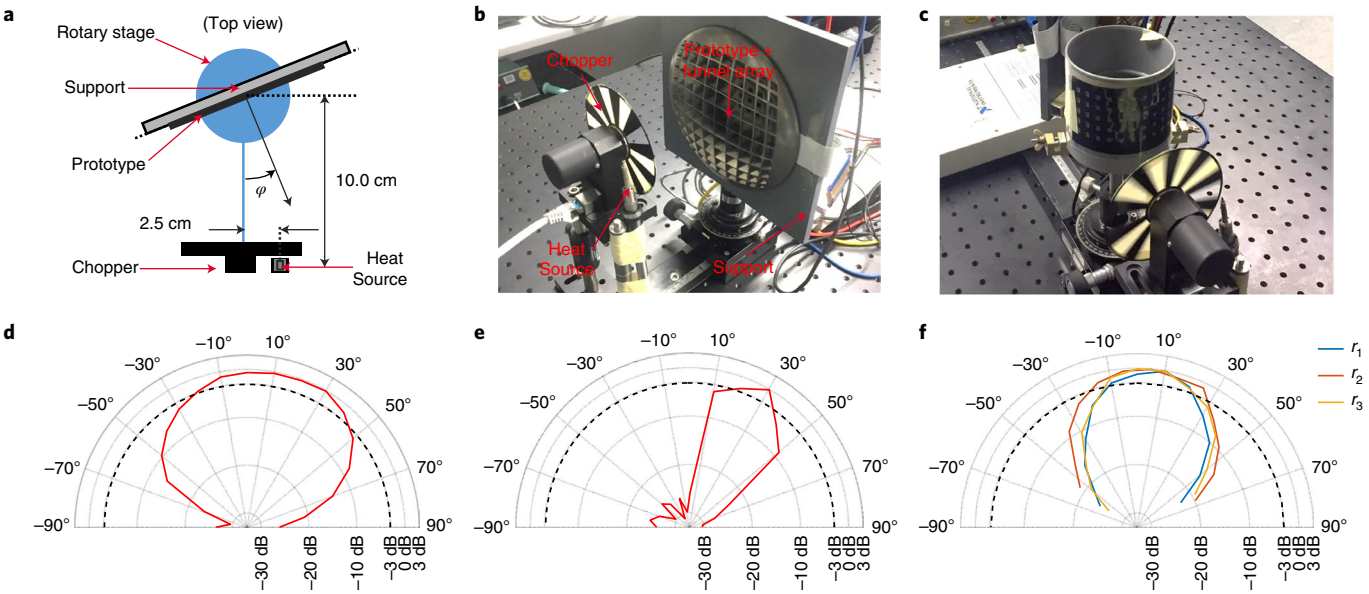

Fig. 4 | Evaluation of directivity detection of the proximity-sensing surface. a,**b**, Simplified diagram (**a**) and photograph (**b**) of the measurement setup used in the directivity detection evaluation. **c**, Photograph of the prototype used in the bending condition. **d**,**e**, Normalized directivity detection pattern recorded using the prototype equipped with (**e**) and without (**d**) the funnel array. **f**, Normalized directivity detection patterns recorded without a funnel array and under three different bending conditions with bending radii $r_1 = 75.0$ mm, $r_2 = 55.0$ mm and $r_3 = 27.5$ mm.

that the CSA preserves the charge between input and output, and combining the result with equation (6), we get

$$\mathrm{SNR} \geq Q_S^2/\overline{Q_{n,\mathrm{out}}^2} = \frac{(p_{\mathrm{pyro}}A_S)^2 \left|\frac{\eta P}{G_T + j\omega H}\right|^2}{\overline{V_A^2}\,(C_{FB}+C_E)^2 + \left(1+\frac{R_{FB}}{R_E}\right) k_B T C_{FB}}. \quad (7)$$

The thermal conductance G_T can be considered, at the first approximation, proportional to the bottom-electrode area[31], which is also roughly equal to the sensor area A_S; therefore, $G_T = G_0 A_S$, where G_0 is a suitable scaling factor. Equation (7) can be further manipulated by introducing parameter α and rewriting C_E according to the sensor capacitance per unit area, C_0. Finally, by assuming that the cut-off frequency introduced by the thermal constant is at a sufficiently higher frequency than the BW, the SNR can be rewritten as

$$\mathrm{SNR} \geq \frac{\frac{p_{\mathrm{pyro}}^2 \eta^2 P_0^2}{G_0^2}}{\overline{V_A^2}\left(\frac{\alpha+1}{\alpha}\right)^2 C_0^2 + \left(1+\frac{R_{FB}}{R_E}\right)\frac{C_0}{\alpha A_S} k_B T}, \quad (8)$$

where P_0 is the irradiance calculated as $P_0 = P/A_S$. Equation (8) reveals that if the integrated noise of the amplifier $\overline{V_A^2}$ is the dominant noise component, the active area of the sensor can be downscaled without lowering the achievable SNR. This is typically the case in CSA implementations based on OTFTs, since these transistors suffer from large low-frequency noise. The minimization of the sensor active area allows the device's thermal time constant to be reduced and enables a higher integration density. However, the minimum sensor area that can be used in the matrix pixel is further limited by feedback capacitance C_{FB}, which must be α times smaller than the sensor capacitance by design. Indeed, as soon as C_{FB} approaches the value of parasitic capacitance at the input of the amplifier, the functionality of CSA is negatively affected. For this reason, C_{FB} should be designed to be sufficiently larger than the input parasitic capacitance of the amplifier. On the other hand, OTFTs with a large channel area should be used to mitigate the impact of their low-frequency noise components, resulting in large stray capacitances and thus larger C_{FB} and even larger sensor capacitance and area. It is, thus, clear that for a given OTFT technology, there exists a trade-off between the minimum sensor area and achievable SNR.

Taking all this into consideration, $C_{FB} = 6$ pF is selected, which for the given ratio α leads to a sensor capacitance of 60 pF, corresponding to a sensor area of 0.37×0.37 cm^2. Following the system specifications for the signal BW (1–10 Hz), the closed-loop cut-off frequency of the CSA needs to be designed to be less than 1 Hz, providing an approximate integration of the input current and thus an output signal proportional to the input charge. Therefore, assuming a target CSA cut-off frequency of 0.1 Hz, this requires $R_{FB} > 300$ GΩ.

A summary of the main system specifications is provided in Supplementary Table 4. The design of the amplifier used in the CSA, its transistor-level schematic (Fig. 1g) and complete AFE implementation in the OTFT technology (Fig. 1h) is discussed in detail in the Supplementary Information.

The proposed system-on-foil design has been complemented with an array of IR-guiding funnels to enhance the directivity and increase the sensitivity of each pyroelectric sensor. For the design of the funnel array, it is assumed that the reflection of the incident radiation on the funnel walls is close to 100%. Ray-tracing simulations have been performed assuming a 1×1 cm^2 Lambertian radiant source (wavelength $\lambda = 10$ μm) placed at 30 cm from the array. The simulation results show that the intensity of the maximum irradiance in the pixels is improved by five times compared with the intensity achieved in the same pixels without the funnel. Moreover, the designed funnel array enables the detection of objects placed even at an angle of $\varphi = 80°$ from normal incidence. Each element of the array exhibits a simulated half-power beamwidth (HPBW) of 30°, a feature that can be exploited to enhance the directional sensitivity of a generic proximity matrix sensor (without the funnel array, HPBW = 85°).

Measurement results. The designed matrix backplane has been fabricated with the technology discussed elsewhere[9] on a 126×126 mm^2 module area (Fig. 2a), obtained from the partitioning of a GEN1

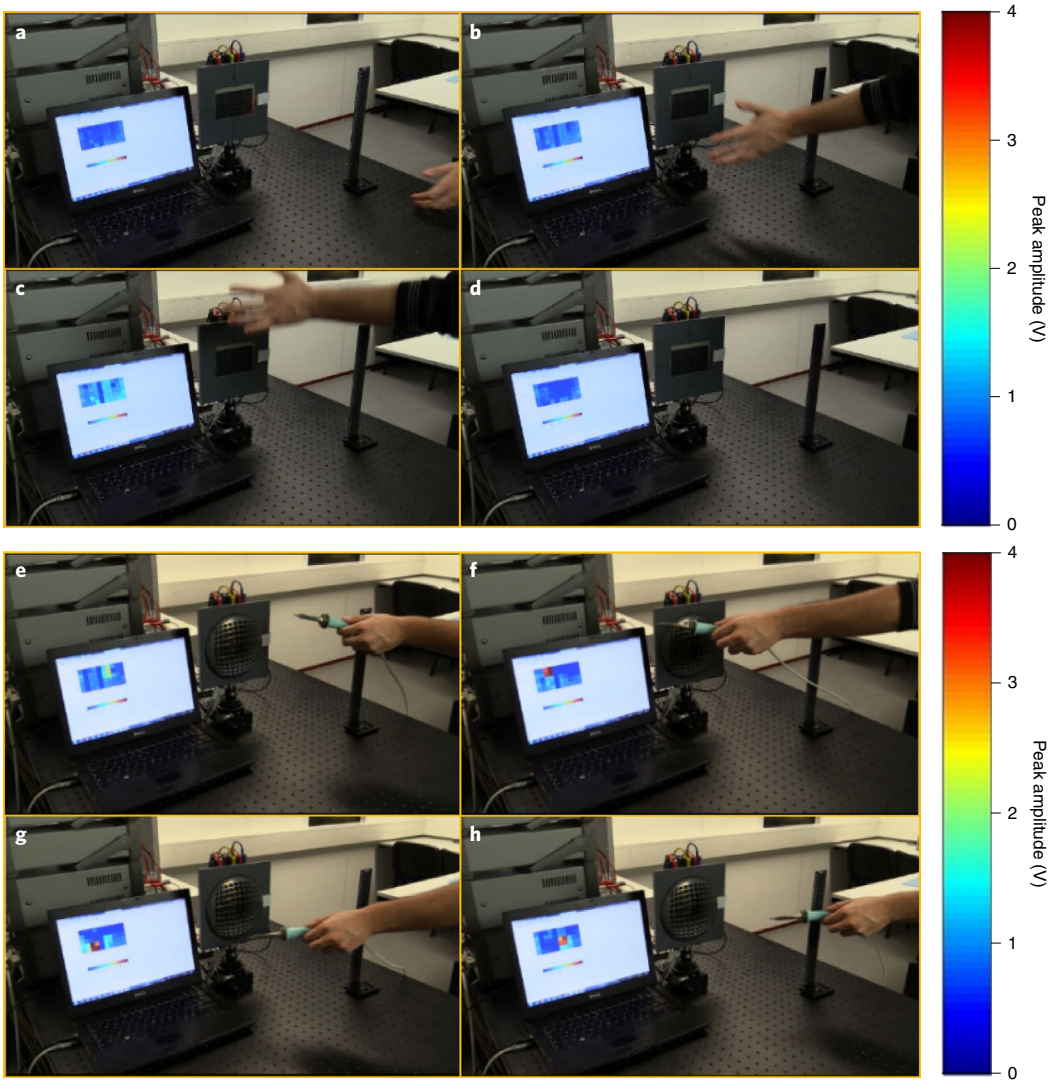

Fig. 5 | Demonstration of human proximity detection (proof of concept). The operator's hand approaches at about 40 cm from the prototype. **a**–**d**, Time sequence of the video frames. The approach of a soldering iron used as the heat source, placed at a distance of 40 cm from the prototype equipped with a funnel array. **e**–**h**, Time sequence of the video frames. The colour map refers to the peak amplitude voltage recorded at the output of each pixel.

plastic substrate. The frontplane (Fig. 2b) has been manufactured too, and the pyroelectric sensors were poled according to the process described elsewhere[8].

The funnel array has been manufactured by means of a three-dimensional (3D) printing process at Joanneum Research (Fig. 2c). To achieve high LWIR reflectivity, the structure was metallized with sputtered aluminium. The funnel array developed with this process is not mechanically flexible. However, this limitation could be overcome by employing flexible materials such as polydimethylsiloxane in combination with a 3D printed mould.

The linearity and current responsivity of the pyro-sensors in the matrix frontplane have been evaluated first using the measurement setup shown in Fig. 3a. The recorded current produced by the sensor versus the incident IR power is plotted in Fig. 3b for both vertical (V) and horizontal (H) polarizations with respect to the surface of the optical bench. The linearity error curves for both polarizations obtained by considering the best-fit linear regression are also presented in Fig. 3b. These measurements highlight that the sensor linearity is nearly independent of the IR polarization and that the maximum relative linearity error is less than 5% over the IR power range of analysis (between −18 and 5 dBm). The measurements are performed using an IR source at 1,550 nm wavelength modulated at 20 Hz frequency (the minimum modulation frequency that could be achieved with the measurement setup). The recorded current responsivity of the pyroelectric sensor is provided in Fig. 3c for both polarizations. The measurement results reveal that the responsivity of the sensor is slightly dependent on the IR polarization. The thermal pole associated with heat capacitance and thermal conductance lies at approximately 70 Hz for the vertical polarization and at 110 Hz for the horizontal one, in both cases well beyond our BW of interest (1–10 Hz). The current responsivity for both polarizations achieves the maximum value of 0.9 μA W^{-1} at a modulation frequency of 1 kHz.

The sensor frontplane is characterized by measuring the remnant polarization, as this parameter determines the pyroelectric coefficient and thus the sensitivity of the sensor. The yield of the sensors in the frontplane is 100% considering nine printed sheets each containing 100 sensors. The sheet-to-sheet variation in the remnant polarization is about 4.0%, expressed in terms of standard deviation normalized to the mean value, which is approximately 70 mC m^{-2}.

Due to the specific design layout, no single sensor analysis of yield and uniformity can be carried out on the sensor matrix.

Table 1 | Main performance indicators measured for the proposed proximity-sensing surface

	Parameter	Symbol	Value	Unit
Front end				
	Gain at 1 Hz		28.1	GV A^{-1}
	Integration bandwidth	f_{C1}–f_{C2}	0.11–62.00	Hz
	Spurious-free dynamic range[a]	SFDR	45.7	dBc
	Equivalent noise charge	ENC	86.2	$ke_{r.m.s.}$
	Noise equivalent power at 20 Hz	NEP	267	nW $Hz^{-1/2}$
	Specific detectivity at 20 Hz	D^*	1.3×10^6	cm $Hz^{1/2}$ W^{-1}
	SNR[b] (bandwidth, 0.1 Hz to 1.0 kHz)		47	dB
	Supply voltage	V_{DD}, V_{SS}	±18	V
	Power consumption		54	µW
	Area		0.5	cm^2
	Required number of devices		15	
	Average yield (over 200 samples)		82	%
Matrix				
	Number of elements		5×10	
	Readout frame rate	F_{RATE}	100	Hz
	Human proximity detection distance		40	cm
	HPBW detection angle[c]		70|20|30	°
	Supply voltage	V_{DD}, V_{SS}	±18	V
	Power consumption[d]		3.2	mW
	Matrix area[d]		50	cm^2
	Minimum tested bending radius	r_3	27.5	mm

[a]At the expected maximum output swing [b]For a maximum amplitude sensor signal of 3 pC [c]Without the funnel array, with the funnel array and under bending conditions (bending radius, r_3 = 27.5 mm) [d]Excluding the five-stage line drivers

Yet, the same technology has been characterized with respect to yield and uniformity for a different design with a sensor area of 2.9 cm^2 and 30 sensors per sheet: under these conditions, the analysis of 14 sheets of sensors (420 samples) revealed a yield of 100% of the sensors, a within-sheet variation in remnant polarization of 1.6% and a sheet-to-sheet variation of 2.5%.

The electrical performance of the AFE circuit has been assessed on test structures (Fig. 2a), which contain the same AFE circuits employed in the backplane pixel. To simplify the characterization of the CSA, this has been performed using the indirect method proposed elsewhere[32]. Here the CSA has been connected as a voltage amplifier (Fig. 3d) by means of an external discrete capacitor with C_S = 68 pF. The frequency response of the circuit is measured by using a 20-mV-peak-amplitude input sinusoidal sweep. The experimental results (Fig. 3e) reveal an in-band gain of 12 V/V, a first cut-off frequency at f_{C1} = 0.11 Hz and a second cut-off frequency at f_{C2} = 62.00 Hz. The gain of the CSA can be indirectly measured from the in-band gain of this voltage amplifier as discussed elsewhere[32]. As a result, the CSA provides a gain of 28.1 GV A^{-1} at 1 Hz. It is worth noting that the measured gain and bandwidth performance are in good agreement with the simulation results (Supplementary Table 5).

The linearity of the voltage amplifier has been evaluated using a 25 $mV_{r.m.s.}$ input single-tone test at 5 Hz (Fig. 3d). This input-signal amplitude is chosen to reach the maximum expected output-voltage swing of the circuit. Indeed, a 3 pC charge is delivered by the pyroelectric sensor as a human approaches it at ~10 cm distance[32]. The recorded output spectrum is presented in Fig. 3f. The circuit linearity is limited by the second harmonic (H2), a result that is not surprising in a single-ended implementation. The spurious-free dynamic range (SFDR) is 45.7 dB. The AFE requires a current consumption of 1.5 µA at supply voltages of ±18 V. Bias voltages V_{B1}, V_{B2} and V_{OFF} are +10, −9 and +10 V, respectively.

The noise performance of the AFE has also been evaluated. It is worth noting that the noise transfer function of the voltage amplifier under test (Fig. 3d) is identical to the one of the CSA in its final application. The recorded output-referred noise power spectral density (Fig. 3g) reveals that the noise floor is dominated, as expected, by the 1/f noise contribution. An output-referred noise of 2.3 $mV_{r.m.s.}$ is obtained by integrating the PSD over the whole measurement bandwidth (0.1 Hz to 1.0 kHz), which is larger than the BW of interest. The integrated noise can also be referred to the input of the CSA in terms of the equivalent noise charge (ENC), multiplying it by the feedback capacitance value of C_{FB} = 6 pF. The corresponding ENC is 12.5 fC or 86.2 $ke_{r.m.s.}$, which further leads to a maximum SNR of 47 dB (assuming 3 pC is the maximum charge delivered by the sensor). The input-referred current noise of the CSA (Fig. 3g) has been numerically fitted with a polynomial expression and used in combination with the current responsivity curve (Fig. 3c) to compute the noise equivalent power (NEP) of the detector (Fig. 3h). The outcome reveals a minimum NEP of 267 nW $Hz^{-1/2}$ at a modulation frequency of 20 Hz. Moreover, considering the active area of the pyroelectric sensor, the proposed detector achieves a specific detectivity of $D^* = 1.3\times10^6$ cm $Hz^{1/2}$ W^{-1} at a modulation frequency of 20 Hz (Fig. 3i).

The functionality of the pyro-matrix backplane is analysed by using frequency-domain measurements. Four complete matrix backplanes have been characterized for a total number of 200 pixels. The defectivity analysis (Supplementary Information) reveals 82% of the fully working pixels over the considered population. The yield value instead reaches 86% when only soft failures are considered.

The frequency responses of the fully working pixels connected as voltage amplifiers (Fig. 3d) are plotted in Fig. 3j. The distribution of the in-band gain (Fig. 3k) reveals a mean value of 12.7 V/V with a standard deviation of 2.0 V/V or 15.7% of the mean value. This result is compatible with the gain desensitization obtained by using closed-loop CSA topology. The observed residual variability is mainly due to the spread of the feedback capacitance value. On the other hand, the distribution of the second cut-off frequency f_{C2} (Fig. 3l) is characterized by a relatively large spread. In this case, the mean value is 96.0 Hz, with a standard deviation of 48.5 Hz or 50.7% of the mean value. The first cut-off frequency, f_{C1}, is typically measured to be below 1.0 Hz. Despite the large variability in the cut-off frequencies, 82% of the analysed CSAs exhibit a 3 dB bandwidth larger than the required bandwidth.

These results are in line with the variability analysis reported in the Supplementary Information, further demonstrating the accuracy of the process design kit developed for this OTFT technology.

The detection directivity of the pyroelectric sensors with and without the funnel array has been also assessed (Fig. 4a–c). Fig. 4e,d shows a comparison of the detection directivity patterns recorded on a pixel (row 3, column 6) using the prototype with and without the funnel array.

It is worth noting that in both recorded detection patterns, the angle that corresponds to the maximum detection value does not coincide with normal incidence (0°). This is mainly due to the 2.5 cm offset of the heat source from the normal direction of the matrix plane (Fig. 4a) corresponding to about 15° of angular misalignment.

This is in line with the measurements shown in Fig. 4d,f. The angular offset visible in Fig. 4e instead is larger than the previous ones. Since the position of the heat source has not been modified between the different experiments, this additional misalignment can be due to an angular offset between the normal to the matrix plane (Fig. 4a) and reference angle of the rotary stage (0°). Indeed, even though the directivity characterization with and without the funnel array has been done in sequence, the matrix and its support have been dismantled from the setup to introduce the funnel array and manually realigned.

The results presented in Fig. 4d reveal that the proximity-sensing capability of the single element exhibits an HPBW value of approximately 70°. The insertion of the funnel array allows to substantially increase the directivity of the sensing elements, leading to HPBW of about 20° (Fig. 4e). On the contrary, the sensitivity improvement highlighted by the simulation results when adding the funnel array has not been experimentally observed. This is mainly caused by the poor coverage of the metallization coating applied to the funnel array, which introduces large losses in the guided radiation. The directivity detection of the matrix pixels has also been investigated under mechanical stress conditions (bending). The prototype without the funnel array has been placed over three cylindrical plastic supports with radii $r_1 = 75.0$ mm, $r_2 = 55.0$ mm and $r_3 = 27.5$ mm. The normalized directivity detection patterns recorded from a generic pixel under three different conditions are shown in Fig. 4f. The measurement results reveal that the directivity of the pixels is modified when bending the plastic substrate. The HPBW under mechanical stress is about half that extracted in the flat state (Fig. 4d), and it is approximately equal to 30°, 40° and 30° for r_1, r_2 and r_3, respectively. The reduction and variability of HPBW under bending conditions can be justified by the geometry of the detector and can be a result of the induced superficial strain.

The two backplanes featuring the highest pixel yield (96% and 84%) have been laminated with the sensing frontplanes (both featuring 100% sensor yield) to create two proximity-sensing matrix prototypes. After the lamination was completed, each prototype suffered an additional failure, leading to a non-working column. The proposed system-on-foil design has been qualitatively evaluated by means of proximity tests performed in two different scenarios (Supplementary Videos 1–3; multiple human hands approach from different directions and at different distances from the pyro-matrix, and tracking of a localized and movable heat source).

The human hand approach is presented in Fig. 5a–d. The operator hand approaches at about 40 cm from the prototype, and proximity detection is displayed on the screen by means of real-time visualization software. In the second experiment, a soldering iron is used as a localized heat source (Fig. 5e–h). The heat source is placed at about 40 cm from the matrix, which is also equipped with a funnel array and is moved in the direction parallel to the sample. The heat source produces a localized spot on the screen, qualitatively proving the effectiveness of the funnel array in enhancing detection directivity.

The main indicators of system performance obtained from the measurements are listed in Table 1. The comparison of this work with the current state-of-the-art works is discussed in the Supplementary Information and the results are summarized in Supplementary Table 6.

Conclusions

We have reported a large-area proximity-sensing surface manufactured using printed organic materials with embedded AFE in each pixel. The use of the AFE is crucial in achieving downscaling of the sensor area without a loss of dynamic range and improving the SNR beyond that of current simple active-matrix solutions. The system-on-foil design integrates a matrix of PVDF–TrFE pyroelectric sensors screen printed on a foil frontplane that is then laminated with a second flexible substrate backplane containing a corresponding matrix of AFE manufactured with printed OTFTs. The developed proximity-sensing surface features 5×10 elements distributed over an area of 5×10 cm^2 with a 1 cm pitch arrangement.

The pyroelectric sensors are read out in the current mode by means of dedicated OTFT CSAs, and multiplexed to the output using a time-division approach. The use of a bootstrapped inverter-based amplifier as the core of the CSA is an effective way to achieve enough gain at reduced complexity in terms of transistor count. The statistical analysis of a large number of AFE circuits reveals that the use of a closed-loop configuration together with passive feedback networks reduces the dependence of the front-end performance on the large OTFT parameter viability. This, together with the low number of transistors used (16 OTFTs per pixel), improves the circuit yield. An average defectivity rate of 18% is observed over a population of 200 measured pixels. The highest number of fully working pixels recorded among the analysed matrix backplanes is 48 out of 50, corresponding to 768 fully functional devices. This result demonstrates one of the largest circuit complexity (in terms of device count) achieved by a printed OTFT circuit to date. With a power consumption of 54 μW, the AFE together with the pyroelectric sensor achieves a minimum NEP of 267 nW Hz$^{-1/2}$ or by considering the sensor active area (0.37×0.37 cm^2), a maximum specific detectivity of $D^* = 1.3 \times 10^6$ cm Hz$^{1/2}$ W^{-1}.

The proposed system-on-foil design has been successfully used for the proximity detection of human hands approaching from different directions and for the position tracking of a localized movable heat source, in both cases up to 40 cm distance from the sources. Our results also show that the detection directivity of the sensor can be enhanced by using a 3D printed IR-guiding funnel array. The use of the funnel array improves the directivity of the single pyroelectric sensor from an HPBW value of 70° down to 20°. These results show that printed electronics can provide low-cost solutions suitable for human proximity-sensing applications, where large-area coverage and detection distances below 1 m are the main requirements.

Methods

Pyroelectric sensor characterization. A simplified representation of the measurement setup used for the characterization of the pyroelectric sensor is shown in Fig. 3a. An external laser (Agilent Technologies B1980A) is used as the IR source at 1,550 nm wavelength. An optical attenuator (ATT) is introduced after the laser to control the IR power of the beam during the characterizations and fed to a polarization controller (PLC) to investigate the sensor response at different polarizations of incident light. Single-mode fibres have been used for the interconnection of optical modules. The beam at the output of the fibre facet is collimated by a lens with 4.4 mm focal length (IR1500 F4.40 NAD 0.65). Next, a linear polarizer (PL; Newport 05P509AR MRS65) is introduced in the optical path at 10 cm distance from the fibre facet. An optical chopper (CH; MC1000 equipped with ten blades) is placed at 12.5 cm distance from the polarizer, to vary the modulation frequency of the IR beam. A Thorlabs MC1000 controller is used to drive the optical chopper. To measure the average power of the IR beam, a photodiode (PD; M25338) is mounted on a linear stage placed at 10 cm distance from the chopper and further connected to an optical meter (ML93B Anritsu). A thermal camera (Xenics Xeva 1.7 320×256 TE1 USB 100) is also temporarily added to the setup at 20 cm far from the chopper to record the beam profile. Under these conditions, the measured beam profile exhibits an HPBW of 750 μm. During the characterizations, the camera is replaced by the frontplane foil containing an array of 10×10 pyroelectric sensors (Fig. 2b) fixed on a plastic support. This measurement setup is initially used to characterize the linearity of the proximity sensor. To do so, the axis of the linear polarizer is first oriented in the direction perpendicular to the optical bench plane and then the IR power is swept starting from +3.5 to −16.5 dBm in steps of 3 dBm by using the attenuator. The current produced by the sensor under test is measured with readout electronics based on off-the-shelf silicon components comprising a transimpedance amplifier and voltage buffer to drive the HP35670 dynamic signal analyser. To estimate the power of the sensor signal from the recorded output spectrum, the first six harmonics are taken into consideration. This experiment has been repeated after rotating the linear polarizer axis by 90°. In both measurements, the optical chopper modulates the IR radiation at a frequency of 80 Hz and the sensor under test belongs to column 3 and row 10. For characterizing the responsivity of the sensor current, the same setup is used. In this case, the average power read by the photodiode is +3.4 dBm, whereas the chopping frequency is swept from 20 Hz to 1 kHz.

The frequency range of analysis is only limited by the MC1000 system. Also, in this case, the characterization of the sensor current responsivity is repeated using two different, orthogonal polarizations.

Sensor frontplane evaluation. The remnant polarization of the sensor matrix on the frontplane is measured during the last manufacturing step—the poling process. The co-polymer is poled by a sinusoidal a.c. field generated by a high-voltage amplifier (AMT-10B10-L) slowly varying at 3–5 Hz at an amplitude increasing from zero to a maximum of 100–150 V μm^{-1} during ten cycles and remaining at the maximum for two cycles. This poling procedure is repeated three times and the remnant polarization is measured from the integral over time of the poling current during the last cycle divided by the poled active area of the sensor. The current is measured at the analogue output of AMT-10B10-L by an NI 6229 data acquisition device, and the accuracy of the remnant polarization value is determined by the accuracy of the sensor area to about 0.5%.

AFE characterization. The frequency response of the AFE circuit in the test structure is measured by means of an HP35670 dynamic signal analyser. A sinusoidal source signal with 20 mV amplitude provided by the analyser is fed to the circuit by using discrete series capacitance $C_S = 68\,\text{pF} \pm 5\%$ (AVX 0805 MLCC), which is used here in place of the pyroelectric sensor to simplify the electrical characterization process (Fig. 3d). It should be noted that the value of C_S differs from the value of C_E calculated at the design stage. Indeed, preliminary measurements performed on the frontplane highlight that the pyroelectric sensors exhibit a typical capacitance of nearly 70 pF, which deviates slightly from the design value.

Matrix backplane evaluation. The frequency response of the AFE contained in each pixel in the backplane is measured by using the same approach described in the previous section. In this case, however, the AMUX is statically addressed to select the desired pixel and excitation (input sinusoidal sweep with 20 mV amplitude) is applied to the AFE electronics by means of a test probe. A printed circuit board is used to connect the matrix backplane with the readout electronics based on off-the-shelf components. Each matrix column voltage V_{CLM} is connected one at a time to a Si voltage buffer amplifier and further fed to the HP35670 dynamic signal analyser.

Directivity analysis. The measurement setup developed for this evaluation exploits a controlled heat source placed at 10 cm distance from the prototype accommodated on a plastic support, and a rotary stage to control the relative angular position φ of the sensing surface with respect to the source (Fig. 4a). The normalized detection diagram is measured by sweeping the angular position φ of the prototype, from −90° to 90° in steps of 10°.

A soldering iron (Weller MT301 tip) together with its temperature control unit (Weller MT1500) is used to realize the temperature-controlled heat source. During the experiments, the soldering iron tip is maintained at a constant temperature of 454 °C. A ten-blade optical chopper is used to modulate the IR radiation of the heat source. A Thorlabs MC1000 controller is used to drive the optical chopper. The chopper together with its controller allow to achieve a minimum modulation frequency of 20 Hz. However, to mitigate the frequency folding introduced by the aliasing of the harmonic components beyond the Nyquist frequency, the modulation frequency is further lowered down to 4 Hz by obscuring eight chopper holes.

A simplified diagram and photograph of the measurement setup are provided in Fig. 4a and Fig. 4b, respectively. The same setup is also used for the directivity detection assessment under mechanical stress conditions. In this case, the prototype is accommodated on a cylindrical plastic support (Fig. 4c). Three different supports featuring radii of $r_1 = 55.0$ mm, $r_2 = 45.0$ mm and $r_3 = 27.5$ mm are used in the setup. The normalized detection diagrams are measured by sweeping the angular position φ of the prototype, from −60° to 60° with steps of 10°.

System-on-foil evaluation. In both experiments, the prototype is placed at a distance of about 40 cm from the heat source. The prototype is read at the target frame rate of 100 frames per second, and the column output voltages are recorded by means of a National Instruments data acquisition board (NI 6259). Real-time visualization software has also been developed to display proximity detection during the experiments.

OTFT characterization. The arrays of OTFTs (Supplementary Figs. 2 and 3 show their electrical characteristics) are measured using an automatic probe station. The devices on foil are connected to a semiconductor parameter analyser (HP B1500A) by means of probes and triaxial cables. The transfer and output characteristics are measured on each device under test in air, dark condition and at room temperature. The transfer characteristics are obtained with a double sweep of the source–gate voltage in the range of [−10.00, 20.00 V] using a uniform step of 0.25 V and for different source–drain voltages (0.10, 1.00, 2.00, 10.00 and 20.00 V). The double-sweep approach is used to detect possible hysteresis in the transistor behaviour, whereas the measurement ranges of the d.c. TFT characteristics are chosen to optimize the OTFT model extraction.

Data availability

All relevant data in this study are available from the corresponding author upon reasonable request.

Received: 18 November 2020; Accepted: 8 April 2022;
Published online: 23 May 2022

References

1. Someya, T. et al. A large-area, flexible pressure sensor matrix with organic field-effect transistors for artificial skin applications. *Proc. Natl Acad. Sci. USA* **101**, 9966–9970 (2004).
2. Someya, T. et al. Cut-and-paste organic FET customized ICs for application to artificial skin. In *2004 IEEE International Solid-State Circuits Conference (IEEE Cat. No.04CH37519)* **1**, 288–529 (IEEE, 2004).
3. Schwartz, G. et al. Flexible polymer transistors with high pressure sensitivity for application in electronic skin and health monitoring. *Nat. Commun.* **4**, 1859 (2013).
4. Yokota, T. et al. Sheet-type flexible organic active matrix amplifier system using pseudo-CMOS circuits with floating-gate structure. *IEEE Trans. Electron Devices* **59**, 3434–3440 (2012).
5. Zirkl, M. et al. An all-printed ferroelectric active matrix sensor network based on only five functional materials forming a touchless control interface. *Adv. Mater.* **23**, 2069–2074 (2011).
6. Fattori, M. et al. Organic pressure-sensing surfaces fabricated by lamination of flexible substrates. *IEEE Trans. Compon. Packag. Manuf. Technol.* **8**, 1159–1166 (2018).
7. Magic Pad in Organic Electronics Association (OE-A) brochure. http://www.isorg.fr/actu/8/magic-pad-in-organic-electronics-association-oe-a-brochure_69.htm (2019)
8. Gold, H. et al. Flexible single-substrate integrated active-matrix pyroelectric sensor. *Phys. Status Solidi RRL* **13**, 1900277 (2019).
9. Fattori, M. et al. A gravure-printed organic TFT technology for active-matrix addressing applications. *IEEE Electron Device Lett.* **40**, 1682–1685 (2019).
10. Cheung, E. & Lumelsky, V. A sensitive skin system for motion control of robot arm manipulators. *Rob. Auton. Syst.* **10**, 9–32 (1992).
11. Wistort, R. & Smith, J. R. Electric field servoing for robotic manipulation. In *2008 IEEE/RSJ International Conference on Intelligent Robots and Systems* 494–499 (IEEE, 2008).
12. Hsiao, K., Nangeroni, P., Huber, M., Saxena, A. & Ng, A. Y. Reactive grasping using optical proximity sensors. In *2009 IEEE International Conference on Robotics and Automation* 2098–2105 (IEEE, 2009).
13. Terada, K. et al. Development of omni-directional and fast-responsive net-structure proximity sensor. In *2011 IEEE/RSJ International Conference on Intelligent Robots and Systems* 1954–1961 (IEEE, 2011).
14. Lumelsky, V. Sensitive skin. *IEEE Sens. J.* **1**, 41–51 (2001).
15. Gelinck, G. et al. Flexible active-matrix displays and shift registers based on solution-processed organic transistors. *Nat. Mater.* **3**, 106–110 (2004).
16. van Lieshout, P. et al. A flexible 240×320-pixel display with integrated row drivers manufactured in organic electronics. In *ISSCC 2005 IEEE International Digest of Technical Papers. Solid-State Circuits Conference* **1**, 578–618 (IEEE, 2005).
17. Raiteri, D. et al. Positive-feedback level shifter logic for large-area electronics. *IEEE J. Solid-State Circuits* **49**, 524–535 (2014).
18. Abdinia, S. et al. Organic CMOS line drivers on foil. *J. Disp. Technol.* **11**, 564–569 (2015).
19. Crone, B. et al. Large-scale complementary integrated circuits based on organic transistors. *Nature* **403**, 521–523 (2000).
20. Fujitsuka, F. et al. Monolithic pyroelectric infrared image sensor using PVDF thin film. In *International Conference on Solid-State Sensors and Actuators* 1237–1240 (IEEE, 1997).
21. Binnie, T. D. et al. An integrated 16×16 PVDF pyroelectric sensor array. *IEEE Trans. Ultrason., Ferroelectr., Freq. Control* **47**, 1413–1420 (2000).
22. Pullano, S. A. et al. A pyroelectric sensor for system-on-a-chip. In *2014 40th Annual Northeast Bioengineering Conference (NEBEC)* 1–2 (IEEE, 2014).
23. Scheipl, G. et al. Fabrication, characterization and modeling of PVDF based organic IR-sensors for human body recognition. *SENSORS 2009 IEEE* 1252–1255 (IEEE, 2009).
24. Chen, X. et al. A flexible piezoelectric-pyroelectric hybrid nanogenerator based on P(VDF-TrFE) nanowire array. *IEEE Trans. Nanotechnol.* **15**, 295–302 (2016).
25. Hossain, A. et al. Pyroelectric detectors and their applications. *IEEE Trans. Ind. Appl.* **27**, 824–829 (1991).
26. Hughes, D. et al. A robotic skin for collision avoidance and affective touch recognition. *IEEE Robot. Autom. Lett.* **3**, 1386–1393 (2018).
27. Xia, F. et al. Tri-mode capacitive proximity detection towards improved safety in industrial robotics. *IEEE Sens. J.* **18**, 5058–5066 (2018).
28. Hasegawa, H. et al. Net-structure proximity sensor: high-speed and free-form sensor with analog computing circuit. *IEEE/ASME Trans. Mechatronics* **20**, 3232–3241 (2015).

29. Fattori, M. et al. Flexible pressure and proximity sensor surfaces manufactured with organic materials. In *2017 7th IEEE International Workshop on Advances in Sensors and Interfaces (IWASI)* 53–58 (IEEE, 2017).
30. Johnson, J. B. Thermal agitation of electricity in conductors. *Phys. Rev.* **32**, 97–109 (1928).
31. Weller, H. J. et al. Low-noise charge sensitive readout for pyroelectric sensor arrays using PVDF thin film. *Sens. Actuators, A* **85**, 267–274 (2000).
32. Fattori, M. et al. Circuit design and design automation for printed electronics. In *2019 Design, Automation & Test in Europe Conference & Exhibition (DATE)* 42–47 (IEEE, 2019).

Acknowledgements

We would like to acknowledge financial support from the European Commission for the projects ATLASS (Horizon 2020, Nanotechnologies, Advanced Material and Production theme, contract no. 636130, to M.F., J.F., E.C., M.C., D.L., S.L., C.L., L.T., S.J, K.R., R.C., H.G., M.A., M.Z., J.G., A.T., M.P., B.L., B.S. and J.S.).

Author contributions

M.F. designed and simulated the system, performed the electrical characterizations together with J.F., and wrote the article with the help of P.H. and E.C. S.C. performed the optical characterization of the pyroelectric sensors. M.C. and R.C. lead the research and development of the OTFT technology on the CEA pilot line. D.L. together with S.L. developed and optimized the gravure-printing process steps. C.L. performed the OTFT electrode fabrication with both photolithography and screen-printing techniques. L.T. carried out the backplane layout optimization and generation of printing mask sets. S.J. and K.R. performed the electrical characterization and data analysis of the OTFTs. H.G. contributed to the design and layout of the sensor frontplane. M.A. manufactured the sensor frontplanes via screen printing. M.Z. and M.P. poled and characterized the uniformity of the sensor frontplane. J.G. and A.T. performed experiments on the pyroelectric sensors and developed a suitable electric model. B.L. designed and simulated the funnel array for the sensor frontplane. B.S. lead the development of the pyroelectric sensor technology. J.S. performed the lamination of the backplane with the frontplane. E.C., M.C., R.C., H.G. and B.S. planned the research.

Competing interests

The authors declare no competing interests.

Additional information

Supplementary information The online version contains supplementary material available at https://doi.org/10.1038/s41928-022-00762-6.

Correspondence and requests for materials should be addressed to Marco Fattori.

Peer review information *Nature Electronics* thanks Jan Genoe and the other, anonymous, reviewer(s) for their contribution to the peer review of this work.

Reprints and permissions information is available at www.nature.com/reprints.

Publisher's note Springer Nature remains neutral with regard to jurisdictional claims in published maps and institutional affiliations.